Relationship between ocean velocity and motionally induced electrical signals:
1. In the presence of horizontal velocity gradients

Zoltan B. Szuts[1,2]

[1] Motionally induced electric fields and electric currents in the ocean depend to first order solely on the vertical dimension. We investigate the significance of two-dimensional (2-D) perturbations that arise in the presence of horizontal velocity gradients. The full electric response is calculated for two schematic geometries that contain horizontal velocity gradients, have a two-layer ocean with a layer of sediment beneath, and are described by four nondimensional parameters. When considered over the realistic ranges of oceanic aspect ratio (the ratio of water depth to the width of velocity), sediment thickness, and sediment conductivity, velocity errors arising from 2-D perturbations are found to be less than a few percent of the dominant one-dimensional (1-D) signal. All errors depend on the aspect ratio to the power of 1.9 (1) for signals induced by the vertical (horizontal) component of the Earth's magnetic field. Depth-uniform velocity errors are proportional to the 1-D sediment conductance ratio, whereas depth-varying velocity errors are independent of sediment thickness or conductivity. Errors are weakly (proportionally) dependent on the jet depth for signals induced by the vertical (horizontal) component of the magnetic field. Two-dimensional perturbations decay away from the forcing region with a half width of 0.2–1 times the 1-D effective water depth. This study extends the first-order theory to the maximum expected aspect ratios for oceanic flow and finds small perturbations with simple dependencies on the nondimensional parameters.

1. Introduction

[2] Measuring horizontal electromagnetic fields (EM) that are generated from the motion of seawater through the Earth's magnetic field is a convenient way to indirectly measure ocean velocity. Observations can be made from a variety of platforms, including submarine cables, bottom-mounted sensors, vertical profilers, and horizontally drifting floats. The technique has unique advantages, and in many cases electric field observations are the only practical means for measuring the desired quantity. For example, EM profiling floats (Expendable Current Profiler (XCP) [*Sanford et al.*, 1982], ElectroMagnetic APEX float (EM-APEX) [*Sanford et al.*, 2007]) are the only current profilers suitable for deployment by aircraft or for shipboard deployment under heavy sea states that prevent normal over-the-side operations [*Girton et al.*, 2001]. Cables or bottom electrometers [*Meinen et al.*, 2002] (Horizontal electric field PIES (HPIES), T. B.

Sanford, personal communication, 2008) measure a time series of spatially integrated absolute velocity that is dynamically similar to transport [*Luther and Chave*, 1993], a measurement that is more expensive to replicate with standard techniques.

[3] The availability of commercial EM instruments (XCP, EM-APEX, or HPIES) and cables indicate a wide accessibility to the oceanographic community. The success of measurements of the transport of the Florida current made over the past 35 years [*Larsen and Sanford*, 1985; *Baringer and Larsen*, 2001] suggests the utility of EM measurements in global observing systems [*Cunningham et al.*, 2007] and cabled observatories. The increasing availability of motional induction techniques, however, necessitates a closer inspection of the underlying theory in a broader range of environments than considered in the literature.

[4] The theory of motional induction that relates ocean velocity to electric fields (EF) and electric currents depends only on the vertical dimension, a one-dimensional (1-D) relationship. This is the form typically used to interpret observations and to calculate water velocity.

[5] The higher-order terms of this theory that depend on velocity or topographic gradients have not yet been directly calculated or observed in situations where they are expected to be significant. Although small horizontal perturbations of

[1]Applied Physics Laboratory and School of Oceanography, University of Washington, Seattle, Washington, USA.
[2]Now at Max-Planck-Institut für Meteorologie, Hamburg, Germany.

velocity and topography were considered by *Sanford* [1971], his use of a perturbation technique means that the solution is strictly valid only for small gradients and cannot be directly applied to regions such as continental slopes or the edges of highly energetic eddies.

[6] Here we are concerned with the structure and magnitude of oceanic electric fields in the presence of strong horizontal gradients of velocity. Electromagnetic solutions are calculated directly for two simplified geometries and are evaluated for the magnitude of perturbation from the first-order theory. In particular, we focus on the errors that arise in calculating velocity from electric field observations in the presence of these higher-order effects. A companion article [*Szuts*, 2010, hereafter SzII] considers the role of sloping topography in generated higher-order EM perturbations. A complementary paper (Z. B. Szuts, in preparation, 2010) analyzes electric field observations collected across the Gulf Stream at Cape Hatteras, North Carolina, USA and considers the same processes discussed here but for observations in a specific and complex location.

[7] The background theory is presented first in section 2, as is the physical basis for higher-order terms. A common method of evaluating the solutions is presented next (section 3), after which the results from the geometries are discussed in sections 4 and 5. The discussion (section 6) generalizes the results for application to realistic situations, and is followed by the conclusion (section 7). Additional synthesis and estimated errors at one study site are contained in the discussion of SzII.

2. Theory

[8] Electric fields occur in the ocean due to the motion of conductive salt water through the Earth's magnetic field; this is generally called motional induction. The thin aspect ratio of the ocean and the assumption of small horizontal gradients of velocity and topography allow for great simplification of the three-dimensional (3-D) governing equations. Although other analyses focus on additional details of oceanic electromagnetism, the results of *Sanford* [1971] are most appropriate for this investigation because his perturbation technique includes the effect of small horizontal gradients. Other theoretical analyses offer discussions of long period waves [*Larsen*, 1968, 1971; *Tyler*, 2005], the influence of deep earth conductivity structure [*Chave and Luther*, 1990], and spherical coordinates [*Tyler and Mysak*, 1995b], among others.

[9] The principal electric fields (**E**) and electric currents (**J**) generated by ocean flow fall into two modes. The traditional and generally more important mode restricts **E** and **J** to the vertical plane. This is a toroidal mode that describes, for instance, electric currents in the surface layer forced by surface flow with weaker electric currents returning in the motionless deep ocean. The magnitude of **E** or **J** depends on the strength of the vertically averaged (defined as barotropic) or vertically varying (defined as baroclinic) velocity signals, respectively. At the simplest, this is exemplified by two cases of an ocean over a nonconductive seafloor: if water motion is vertically uniform, **E** is maximal and **J** is zero everywhere, in analogy to the Hall effect of classical physics; while if water motion is purely baroclinic there is no **E** but **J** is maximal.

[10] The second mode, called poloidal, is characterized by **E** that uniformly fill the water column and are directed in the horizontal plane. This mode only exists in situations where there are gradients in the downstream direction and thus is a 3-D effect. Such effects, often called nonlocal currents, will not be discussed further [see *Tyler et al.*, 1997, 2003; *Flosadóttir et al.*, 1997].

2.1. General Solution

[11] *Sanford* [1971] solves for a general solution that makes use of a number of assumptions. The first-order solution he obtained is now well established [*Chave and Luther*, 1990; *Tyler and Mysak*, 1995a]. Although the analytic form of the higher-order terms is specific to his assumptions, it suggests the underlying physical factors relating the EM solution to perturbations of velocity and topography. The assumptions he made are: a horizontal ocean bottom (H) with small topographic perturbations (h, where $h/H \ll 1$), width scales (L) much larger than bottom depth ($H/L \ll 1$), predominantly horizontal oceanic velocity ($\mathbf{v} = (u, v, 0)$), distant lateral boundaries, a layer of underlying sediment that has a uniform electrical conductivity, and a highly conductive deep earth to approximate the deep but conductive mantle.

[12] Although it is readily shown that time variations of motionally induced **E** in turn induce magnetic fields that are negligible compared to the Earth's magnetic field, a less evident process is inductive coupling between the ocean and the conductive mantle. The strength of inductive coupling depends on both the frequency and the spatial extent of oceanic flow, and has been shown to be small (<5%) for ocean flows that are smaller than basin scale (<1000 km) and slower than tidal frequencies [*Sanford*, 1971; *Chave and Luther*, 1990]. These constraints will be used here to define the quasi-static form of motional induction.

[13] In general form, the quasi-static horizontal electric field $\mathbf{E}_h$ is

$$-\mathbf{E}_h = \nabla_h \phi = \mathbf{v} \times \hat{k} F_z - \mathbf{J}_h/\sigma, \tag{1}$$

where ∇_h is the horizontal gradient operator, ϕ is electric potential, $\mathbf{v}$ is oceanic velocity, F_z is the vertical component of Earth's magnetic field, $\hat{k}$ is the vertical unit vector (pointing upward), σ is electrical conductivity, and $\mathbf{J}_h$ is horizontal electric current density. The electromotive driving force $\mathbf{v} \times \hat{k} F_z$ is what generates electric field and electric currents.

[14] A general form for horizontal electric current density divided by conductivity with the above assumptions is [*Sanford*, 1971]

$$\frac{\mathbf{J}_h}{\sigma} = (\mathbf{v} - \overline{\mathbf{v}}^*) \times F_z \hat{k}$$

$$- \nabla_h \left\{ \frac{1}{H(1+\lambda)} \int_{-H}^{\zeta} \hat{k} \cdot (\mathbf{v} \times \mathbf{F}) z' \, \mathrm{d}z' + \int_{-H}^{z} \hat{k} \cdot (\mathbf{v} \times \mathbf{F}) \, \mathrm{d}z' \right\},$$

$$\tag{2}$$

with

$$r = \sqrt{(x-x')^2 + (y-y')^2}$$

$$D = H + \zeta - h + \frac{\sigma_s}{\sigma}(H_s - H + h) \tag{3}$$

$$\overline{\boldsymbol{v}}^* = \int_{-H+h}^{\zeta} \sigma \boldsymbol{v}\, dz' \Big/ \int_{-H_s}^{\zeta} \sigma\, dz',$$

where ζ is the sea surface, $-H$ is the mean position of the seafloor, h is the perturbation of the seafloor, $-H_s$ is the bottom of conductive sediment, D is a scaled water depth, σ_s is the uniform sediment conductivity, λ is the sediment conductance factor ($D/H = 1 + \lambda$), and $\overline{\boldsymbol{v}}^*$ is the conductivity-weighted vertically averaged velocity. The coordinate directions are x is positive east, y is positive north, and z is positive upward. The first and second terms on the right-hand side of (2) represent first-order and higher-order processes. The addition of a third term caused by 3-D effects makes $\boldsymbol{J}_h$ nondivergent to order H^2/L^2 [Sanford, 1971].

2.1.1. First-Order Term

[15] The first term on the right-hand side of (2) is the principal toroidal mode. This term is one-dimensional because it only depends on the vertical dimension: a vertical integral of velocity (3) defines the depth-uniform electric field $\overline{\boldsymbol{v}}^* F_z$, while vertical variations of $\sigma(\boldsymbol{v}(z) - \overline{\boldsymbol{v}}^*)$ determine the electric current density. The 1-D approximation used to interpret observations is obtained by keeping only this term, which is interchangeably called 1-D or first order.

[16] The quantity $\overline{\boldsymbol{v}}^*$ corresponds physically to the vertically uniform horizontal electric field divided by F_z and is called the vertically averaged conductivity-weighted velocity. In the 1-D approximation, the constraint that $\boldsymbol{J}_h$ must vertically integrate to zero to conserve charge leads to the definition of $\overline{\boldsymbol{v}}^*$.

[17] The electric current density divided by σ is the difference between that driven by the depth-uniform electric field and that generated by local horizontal water motion, $(\boldsymbol{v}(z) - \overline{\boldsymbol{v}}^*) \times \hat{\boldsymbol{k}} F_z$. In the limiting situation where the flow field is entirely barotropic and there is no sediment layer, there will be no electric currents.

[18] A simpler definition of $\overline{\boldsymbol{v}}^*$ is obtained by simplifying the numerator and denominator of (3). A Reynolds decomposition of the numerator defines the vertical correlation factor γ

$$\frac{1}{H - h + \zeta} \int_{-H+h}^{\zeta} \sigma \boldsymbol{v}\, dz = \overline{\sigma \boldsymbol{v}} = \overline{\sigma}\,\overline{\boldsymbol{v}} + \overline{\sigma'\boldsymbol{v}'} = \overline{\sigma}\,\overline{\boldsymbol{v}}(1+\gamma), \tag{4}$$

where for the variables $\boldsymbol{v}(z)$ and $\sigma(z)$, $\overline{\boldsymbol{v}}$ and $\overline{\sigma}$ indicate a vertical average in the water column and $\boldsymbol{v}'$ and σ' indicate perturbations about the vertical mean.

[19] Dividing the denominator by the vertical conductance of the water column and rearranging gives

$$1 + \lambda = \int_{-H_s}^{\zeta} \sigma(z)\, dz \Big/ \int_{-H+h}^{\zeta} \sigma(z)\, dz$$

$$= 1 + (H_s - H + h)\sigma_s / (H - h + \zeta)\overline{\sigma}, \tag{5}$$

where λ is the bottom conductance factor, the ratio of the sediment conductance to the water column conductance.

[20] Combining (4) and (5) yields a simplified form of $\overline{\boldsymbol{v}}^*$ more suitable for interpreting observed $\boldsymbol{E}$

$$\overline{\boldsymbol{v}}^* = \overline{\boldsymbol{v}}\left(\frac{1+\gamma}{1+\lambda}\right). \tag{6}$$

Although this form has no horizontal dependence because of the assumption of $H/L \ll 1$, Chave and Luther [1990] show that the variables $\overline{\boldsymbol{v}}^*$, γ, and λ are horizontally averaged within a few times the water depth.

[21] The factor λ quantifies the amount of shorting through the bottom sediment. The physical meaning of it is clarified by the definition of D, equation (3), or $D = H(1 + \lambda)$. The scaled bottom depth D is the depth of the water column plus a thickness of seawater with the same conductance as the sediments. Thus, the barotropic velocity generates an electric field that is reduced by the additional conductance of the seafloor.

[22] By parameterizing conductive sediment with λ, we make the simplifying assumption that the sediment can be treated as a layer with uniform conductivity σ_s. In reality, conductivity depends on the porosity of sediment, the interstitial fluid (typically salt water, but possibly less conductive substances such as fresh water or gas hydrates), and the type of sediment. Salt water is the most common pore fluid, and, combined with a decrease in porosity with depth due to compaction, sediment conductivity is expected to decrease logarithmically in the sediment column via Archie's Law [Simpson and Bahr, 2005]. Despite these general trends, sediment conductivity is a poorly characterized variable outside of commercial exploration geophysics. Total sediment conductance can be estimated on the scale of sedimentary basins from sediment thickness [Flosadóttir et al., 1997; Tyler et al., 1997] or from detailed and local geophysical data [Szuts, 2008]. As far as concerns the first-order response, the use of λ emphasizes that it is the total conductance of the sediment column that matters, and not its breakdown into either average conductivity or thickness.

[23] The vertical correlation factor $\gamma = \overline{\sigma'\boldsymbol{v}'}/\overline{\sigma}\,\overline{\boldsymbol{v}}$ corrects for vertical correlations of velocity and water conductivity that alter the electric field $\overline{\boldsymbol{v}}^* F_z$. For instance, if a layer of fast moving water (large motional induction source) is also more conductive, then that layer drives a larger electric current at that depth compared to a uniformly conductive case. The larger electric current in turn generates a larger electric field. The sign of γ is positive in this case, and $\overline{\boldsymbol{v}}^*$ is accordingly larger. Measurements of temperature and salinity simultaneous with $\boldsymbol{J}_h/\sigma$ allow direct calculation of γ, or it can be estimated from nearby or historic profiles [Luther and Chave, 1993]. Prior calculations of γ found it to have less than a 10% influence on $\overline{\boldsymbol{v}}^*$ for open ocean baroclinic modes, with large values only occurring in strong baroclinic flows [Chave and Luther, 1990; Szuts, 2004].

2.1.2. Higher-Order Term: Horizontal Gradients

[24] The second term on the right-hand side of (2) is a higher-order term because it scales as H/L. It is also two-dimensional (toroidal) because it couples with a term of similar form for J_z (not shown). The poloidal mode (not shown) also scales as H/L but describes 3-D effects.
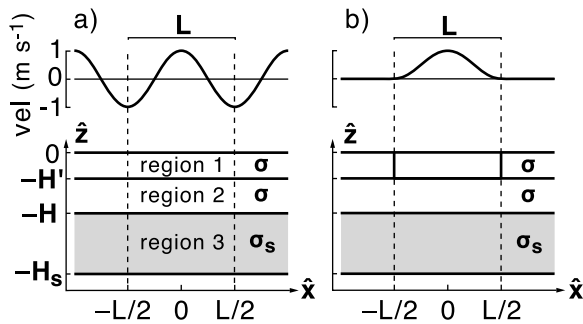
Figure 1. Geometries for which magnetostatic solutions are calculated, both with three layers: a surface ocean jet (region 1), a motionless deep ocean (region 2), and a layer of conductive sediment (region 3). The top layer moves into the page (positive $\hat{y}$) with the vertically uniform velocity shown in the top. (a) Sinusoidal geometry (see section 4), with (top) an infinite sinusoidal velocity and (bottom) 3 horizontal layers. (b) Cosine jet geometry (see section 5), with (top) a finite cosine jet velocity and (bottom) the same 3 horizontal layers. The 6 parameters that define each geometry are shown in bold.

[25] The second term is nonzero if there are horizontal gradients of H, λ, F or velocity. It includes both depth-uniform and depth-varying components (the first and second integrals of term 2, respectively). In analogy with the horizontal averaging of the first-order term, it is expected that the higher order terms depend on a region within a few times the water depth. The H/L scaling explains why the 1-D approximation is sufficiently accurate for the small aspect ratios typically found in the open ocean.

[26] In highly energetic regions that are often of interest to physical oceanographers, however, H/L is not necessarily $\ll 1$. The perturbation technique used to obtain (2) is not valid for situations that break the initial assumptions, and to accurately calculate the EM response under such conditions it is necessary to calculate solutions with alternative techniques.

2.2. Sampling Techniques

[27] To be able to apply our results to interpreting electromagnetic observations, we must discuss briefly how field measurements are obtained. Most common methods for obtaining velocity use electrodes, although for other purposes the magnetic field is also relevant. Electrodes can be mounted on two broad types of platforms: a stationary platform or one that drifts freely in the horizontal plane.

[28] Stationary platforms such as cables or bottom electrometers measure the electric field, which in the 1-D approximation is equivalent to $\bar{v}* \times \hat{k}F_z$. For stationary electrodes the local velocity in (1) ($v \times F$) cancels that in the first term of J_h/σ, leaving only the electric fields caused by $\bar{v}*$ and higher-order terms.

[29] Untethered floats such as Lagrangian drifters (e.g., EM-APEX) or vertical profilers (e.g., XCP) move horizontally at the local unknown water velocity. The electric potential across the instrument body comes from the electric current density divided by σ. Instruments with an elongated shape are insensitive to small relative motion between the instrument and the local water [*Sanford et al.*, 1978]. The measured signal is equivalent to $(v(z) - \bar{v}*) \times \hat{k}F_z$ in the 1-D

approximation, with possible contributions from higher-order terms.

[30] Any independent and absolute measurement of the horizontal velocity can be used to reference the relative velocity of a float, from which the absolute velocity profile and $\bar{v}*$ can be recovered. Some instruments include a secondary velocity sensor, such as a bottom-reflecting acoustic Doppler velocity sensor on the Absolute Velocity Profiler (AVP) [*Sanford et al.*, 1985] or the RAFOS tracking for an electrode-equipped RAFOS float (Electric Field Float) [*Szuts*, 2004], or surface GPS fixes for a multicycle EM-APEX float. Independent but concurrent velocity measurements can also be used, such as shipboard ADCP profiles for XCPs [e.g., *Girton et al.*, 2001].

[31] In analogy to the two types of measurements that can be made, the higher-order cases presented below will be evaluated for the perturbations of the depth-averaged E and the depth-varying J/σ from the dominant 1-D signal. These two aspects of the solution are further appealing because they correspond to the decomposition of velocity into barotropic and baroclinic components.

3. Approach for Resolving Higher-Order Electric Fields

[32] Because of the difficulty of obtaining general analytical forms for arbitrarily large gradients of velocity or topography, we instead consider limited geometries that contain horizontal velocity gradients in a two-dimensional plane. The solutions are technically magnetostatic, because continuously flowing charge in J generates magnetic fields (magneto-) and because the quasi-static approximation excludes inductive coupling between J and B (static).

3.1. Schematic Geometries

[33] Two geometries are considered that both have three layers (Figure 1): a surface ocean that is in motion, a motionless deep ocean, and a mildly conductive sediment layer. The surface layer has a vertically uniform velocity that varies with the cross-stream coordinate. The velocity in the first geometry is sinusoidal and extends to infinity, while that of the second takes the shape of a cosine over a finite region and is zero outside this. These geometries will thus be referred to as 'sinusoidal' or 'cosine jet'. Each is described by four nondimensional parameters, which are varied systematically to obtain solutions over the four-dimensional parameter space. The results from each geometry are discussed in sections 4 and 5.

[34] Although the results are analyzed based on the nondimensionalized parameters, the solutions are calculated with realistic values for each parameter. The maximum velocity v_0 of the surface layer is set at 1 m s^{-1}, an appropriate value for energetic flows in the ocean. The equations are linear with respect to v_0, so this choice is without loss of generality.

[35] The Earth's magnetic field is set to be representative of midlatitude northern hemisphere values: $F_z = -40{,}000 \text{ nT}$, $F_h = 20{,}000 \text{ nT}$. The vertical component F_z induces the dominant signal as well as a two-dimensional (2-D) perturbation, whereas the horizontal component F_h only induces a 2-D perturbation. For reasons related to the geometries chosen, the F_h-induced perturbation is only considered for the cosine jet geometry.

[36] Implicitly assumed by the three-layer geometry is a nonconductive crust underlying the sediment layer. Realistically, the crust has conductivities of 0.0001–0.03 S m^{-1} [*Chave et al.*, 1992; *Simpson and Bahr*, 2005], which is at least an order of magnitude smaller than typical sediment conductivity and does not support a significant flow of electric current for the motionally induced signals considered here.

3.2. Calculating 2-D Perturbations

[37] The 2-D solutions can be considered as the sum of the expected signal from the first-order solution plus a 2-D perturbation: the depth-uniform signal is contained in E, while the depth-varying signal is contained in J/σ. Perturbations generated by F_h are defined in section 5.2.2. The magnitude of the perturbation is the primary focus, but its shape is also considered by the decay half width of the perturbations.

3.2.1. Depth-Uniform Mode

[38] The depth-uniform mode is the vertically uniform electric field ($\bar{v}*F_z$) defined in (6). In the 1-D approximation it is driven by the vertically averaged velocity ($\bar{v}$) with proportionality factors due to sediment conductance (λ) and vertical correlations of conductivity and velocity (γ). Although in general the baroclinic correlation is removed from $\bar{v}*$ by dividing by $1 + \gamma$, the choice of uniformly conductive oceans makes this factor zero in the three geometries.

[39] For 2-D situations E_x is no longer vertically uniform, so a 2-D quantity $\bar{v}_{2\text{-D}}^*$ is calculated by averaging E_x in the water column and dividing by F_z. Although this quantity has physical units of m s^{-1}, it must be corrected for the effective sediment shorting to be directly analogous to the physically relevant quantity $\bar{v}$. In analogy to the 1-D approximation, then, the quantity $\bar{v}_{2\text{-D}}^*$ can be related to $\bar{v}$ by a 2-D quantity $\lambda_{2\text{-D}}$ according to $\bar{v}_{2\text{-D}}^* = \bar{v}/(1+ \lambda_{2\text{-D}})$.

[40] In terms of calculating a depth-uniform perturbation, however, $\lambda_{2\text{-D}}$ is not known a priori. As the electrical properties of the sediment are fully known for our solutions, the 1-D approximation of $\lambda_{1\text{-D}} = (H_s - H)\sigma_r/H$ is the most obvious way to correct $\bar{v}_{2\text{-D}}^*$. When $\lambda_{1\text{-D}}$ is not known, alternative techniques can recover λ (see section 5.2.2 or *Szuts* [2008]).

[41] The depth-uniform perturbation (in m s^{-1}) is thus defined as

$$\bar{\delta}(x) = \bar{v}(x) - \bar{v}_{2\text{-D}}^* (x) (1 + \lambda_{1\text{-D}}). \tag{7}$$

This quantity decreases to 0 as $H/L \to 0$. To obtain one number that characterizes the magnitude of the depth-uniform error for a given set of parameters, we define a depth-uniform error ϵ by calculating the standard deviation of $\bar{\delta}$ over the region $|x| < L/2$. Relative errors are found by dividing by $\bar{v}$, or vH'/H.

3.2.2. Depth-Varying Mode

[42] The depth-varying perturbation is the difference between J/σ predicted by the 1-D approximation and the 2-D solution. Cast into units of velocity, the 2-D perturbation is

$$\delta'(x,z) = v(x,z) - \frac{J_x(x,z)}{\sigma(z)F_z} - \bar{\delta}'(x). \tag{8}$$

A vertical mean $\overline{\delta'}$ is subtracted to remove the influence of the depth-uniform mode

$$\overline{\delta'}(x) = \frac{1}{H} \int\limits_{-H}^{0} \left[v(x,z) - \frac{J_x(x,z)}{\sigma F_z} \right] \mathrm{d}z. \tag{9}$$

Relative perturbations are obtained by scaling with the maximum velocity $v_0 = 1$ m s^{-1}.

[43] The vertical dimension of δ' is compressed by taking the vertical second moment δ'_{std}

$$\delta'_{\text{std}}(x) = \left(\frac{1}{H} \int\limits_{-H}^{0} \delta'^2 \, \mathrm{d}z \right)^{1/2}. \tag{10}$$

The magnitude of depth-varying perturbations is characterized by definition of a depth-varying error ϵ', calculated by the second moment of δ'_{std} over $|x| < L/2$.

[44] In practice, the correction to absolute velocity $\overline{\delta'}$ is usually calculated from reference velocities collected over less than the full water column, adding a potential bias to the depth-varying velocity error. For instance, shipboard ADCP velocities used to reference XCPs are only obtained in the upper 300–700 m of the water column [*Girton et al.*, 2001]. The second moment and maximum velocities can be recalculated using the alternate expressions

$$\delta'_{\text{bias}}(x,z) = v(x,z) - \frac{J_x(x,z)}{\sigma(z)F_z} - \overline{\delta'_{\text{bias}}}(x)$$

$$\overline{\delta'_{\text{bias}}} = \frac{1}{H_2 - H_1} \int\limits_{-H_1}^{-H_2} \left[v(x,z) - \frac{J_x(x,z)}{\sigma(z)F_z} \right] \mathrm{d}z \tag{11}$$

$$\delta'_{\text{std,bias}} = \left(\frac{1}{H} \int\limits_{-H}^{0} \delta'^2_{\text{bias}} \, \mathrm{d}z \right)^{1/2}.$$

The integration limits used here are chosen to represent an XCP referenced with a 150 kHz shipboard ADCP, $H_1 = -300$ m and $H_2 = -50$ m. Similar results are obtained with integration limits representative of other instruments, such as middepth referencing (EFF) [*Szuts*, 2004] or near-bottom referencing (AVP) [*Sanford et al.*, 1985].

3.2.3. Horizontal Averaging Scales

[45] Aside from its magnitude, the horizontal distance that the perturbation $\bar{\delta}$ or δ'_{std} spreads is one way to consider the shape of the perturbation. Because the perturbations are forced to follow the velocity disturbance width scale within $|x| < L/2$, passive spreading is calculated outside of this region.

[46] Specifically, the half width is defined as the distance away from the origin in which the perturbation at $x = \pm L/2$ is reduced by half. This is denoted $L_{\bar{\delta}}$ and $L_{\delta'}$ for the depth-uniform and depth-varying perturbations. If H/L is large enough, the local velocity error maximum can occur outside of $|x| < L/2$, in which case the half width is the distance in which the maximum is reduced by half.

4. Sinusoidal Velocity

[47] The electromagnetic solution for three horizontal layers can be solved analytically if the velocity varies as a

sinusoid (Figure 1a). The top layer is a surface jet over $-H' \leq z \leq 0$ with a vertically uniform velocity $\boldsymbol{v}(x) = v_0 \cos(\alpha x)\hat{\boldsymbol{y}}$ that extends to $x = \pm\infty$, the underlying water is motionless over $-H < z \leq -H'$, and there is a conductive sediment layer beneath ($-H_s < z \leq -H$). The wave number is $\alpha = 2\pi/L$, where L is the wavelength of the velocity forcing. The ocean and sediment each have uniform conductivities of σ and σ_s.

[48] Three nondimensional scales can be formed from the four spatial scales L, H', H, H_s. Nondimensional parameters arise in the solutions by normalizing the vertical scales with L (or $1/\alpha$). As the solution only depends on the relative magnitude of the vertical scales, however, we normalize the vertical scales by H instead to obtain more intuitive nondimensional parameters. Thus, there are 4 nondimensional scales for this geometry: the aspect ratio H/L, the relative depth of the jet H'/H (≤ 1), the relative thickness of the sediment ($H_s - H)/H$, and the relative conductivity $\sigma_r = \sigma_s/\sigma$.

4.1. Solution Method

[49] The magnetostatic solution is obtained by solving Ohm's law for ϕ defined in the standard form ($\boldsymbol{E} = -\nabla\phi$), with constraints coming from Maxwell's equations of continuity of ϕ, continuity of J_z, and zero flow of J_z at the upper and lower boundaries $z = 0, -H_s$. The form of the solution is readily found that meets $\nabla \cdot \boldsymbol{E} = 0$ and the upper and lower boundary conditions, with the unknown coefficients determined algebraically from the internal continuity conditions. The full solution is

$$
\begin{aligned}
\phi_1 &= C_z\left[1 - \frac{\text{scpcs}(\alpha(H - H'))}{\text{scpcs}(\alpha H)}\cosh(\alpha z)\right] \\
&\quad + C_x\left[\frac{\text{ccpss}(\alpha(H - H')) - \text{ccpss}(\alpha H)}{\text{scpcs}(\alpha H)}\cosh(\alpha z)\right. \\
&\quad \left. - \sinh(\alpha z)\right] \\
\phi_2 &= C_z\sinh(\alpha H')\left[\frac{\text{ccpss}(\alpha(z + H))}{\text{scpcs}(\alpha H)}\right] \\
&\quad + C_x[\cosh(\alpha H') - 1]\frac{\text{ccpss}(\alpha(z + H))}{\text{scpcs}(\alpha H)} \\
\phi_3 &= C_z\sinh(\alpha H')\frac{\cosh(\alpha(z + H_s))}{\text{scpcs}(\alpha H)} \\
&\quad + C_x[\cosh(\alpha H') - 1]\frac{\cosh(\alpha(z + H_s))}{\text{scpcs}(\alpha H)}.
\end{aligned} \tag{12}
$$

[50] The three regions correspond to those in Figure 1a. For notational brevity the following definitions are used:

$$
\begin{aligned}
C_z &= \frac{v_0 F_z}{\alpha}\sin(\alpha x) \\
C_x &= \frac{v_0 F_x}{\alpha}\cos(\alpha x) \\
\text{scpcs}(a) &= \sinh(a)\cosh(\alpha(H_s - H)) \\
&\quad + \sigma_r\cosh(a)\sinh(\alpha(H_s - H)) \\
\text{ccpss}(a) &= \cosh(a)\cosh(\alpha(H_s - H)) \\
&\quad + \sigma_r\sinh(a)\sinh(\alpha(H_s - H)),
\end{aligned} \tag{13}
$$

where the last two definitions are for any variable a. The fields $\boldsymbol{E}$, $\boldsymbol{J}$, and $\boldsymbol{B}$ are calculated from Ohm's Law and $\nabla \times \boldsymbol{B} =$ $\mu\boldsymbol{J}$. The electric current stream function ψ, defined as $\boldsymbol{J} = \nabla \times \psi$, is simply a multiple of $\boldsymbol{B}$.

4.2. Results

[51] Initial evaluation of the solution can be done directly with the solutions for E_x and J_x (not shown). We limit the analysis to the depth-uniform mode induced by F_z, however, because the depth-varying mode does not approach the 1-D approximation in the small wave number limit. The presence of adjacent regions of oppositely signed velocity always generates connecting cells of $\boldsymbol{J}$ regardless of wave number. In particular, elliptical cells of $\boldsymbol{J}$ are strongest at $z = -H'$ even for $H/L \ll 1$, instead of becoming nearly horizontal and evenly distributed in the two ocean layers as expected for the 1-D approximation. Similarly, vertical cells from the contribution of F_h are present for all wave numbers. These difficulties are not present in the second geometry, which makes use of bounded velocity signals.

[52] To calculate the depth-uniform perturbation a two-dimensional λ is defined as

$$
1 + \lambda_{2\text{-D}} = \frac{\bar{\boldsymbol{v}}}{\bar{\boldsymbol{v}}^*_{2\text{-D}}} = \frac{\bar{\boldsymbol{v}}F_z}{\bar{E}_x}. \tag{14}
$$

Calculated exactly from E_x by vertically averaging in the water column, $\lambda_{2\text{-D}}$ is

$$
\begin{aligned}
\frac{1}{1 + \lambda_{2\text{-D}}} &= 1 + \frac{1}{\alpha H'}\sinh(\alpha H')\sinh(\alpha(H_s - H))(-\sigma_r)/ \\
&\quad \Big[\sinh(\alpha H)\cosh(\alpha(H_s - H)). \\
&\quad + \sigma_r\cosh(\alpha H)\sinh(\alpha(H_s - H))\Big].
\end{aligned} \tag{15}
$$

[53] The quantity $\lambda_{2\text{-D}}$ has two properties: an independence on x indicates that $\boldsymbol{E}$ is in phase with v, even though $\bar{\boldsymbol{v}}$ or $\bar{\boldsymbol{v}}^*$ in (14) may be small or even 0; and $\lambda_{2\text{-D}}$ is always less than or equal to $\lambda_{1\text{-D}}$. The second property is equivalent to stating that $\bar{\boldsymbol{v}}^*_{2\text{-D}} \geq \bar{\boldsymbol{v}}^*_{1\text{-D}}$. Alternatively, $\lambda_{2\text{-D}}$ can be defined by averaging E_x over the water depth and the sediment, in which case $\lambda_{2\text{-D}} \geq \lambda_{1\text{-D}}$. The physical meaning is the same for either definition of $\lambda_{2\text{-D}}$: in the presence of 2-D perturbations, $\boldsymbol{E}$ is larger in the water column relative to that expected from the 1-D approximation, while in the sediments $\boldsymbol{E}$ is weaker by a greater amount. Averaging only over the water column is preferred, however, because observations can only be made in the water column.

[54] The small wave number limit of (15) should converge to the 1-D theory when $1/\alpha$ is much greater than H', H, and H_s. For comparison, the 1-D $\bar{\boldsymbol{v}}^*$ is $\bar{\boldsymbol{v}}/(1 + \lambda_{1\text{-D}})$, where $\lambda_{1\text{-D}} = (H_s - H)\sigma_r/H$ from (5).

[55] The small wave number limit is obtained from (15) by keeping the first term of Taylor expansions for the hyperbolic trigonometric functions. It is straightforward to show that the 1-D form is obtained. The governing vertical scale arises as the small wave number limit of

$$
\begin{aligned}
D_{2\text{-D}} &\equiv \frac{1}{\alpha}\sinh(\alpha H)\cosh(\alpha(H_s - H)) \\
&\quad + \frac{\sigma_r}{\alpha}\cosh(\alpha H)\sinh(\alpha(H_s - H)),
\end{aligned} \tag{16}
$$
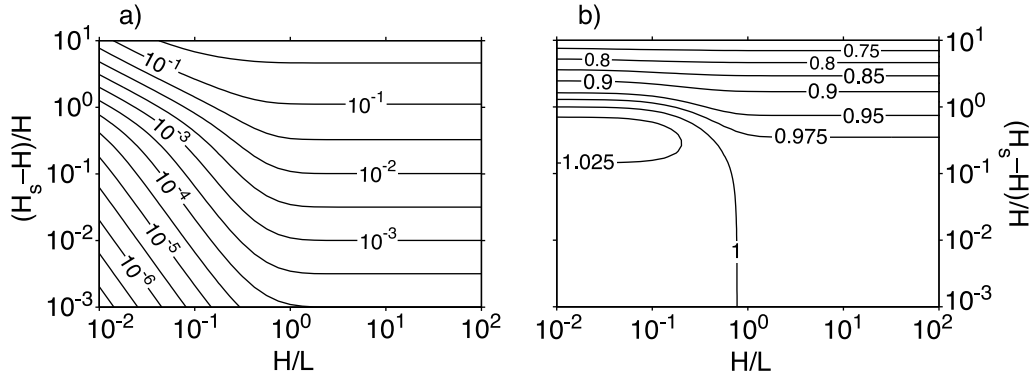
Figure 2. The depth-uniform relative velocity perturbation $|\overline{\delta}/\overline{v}|$ from (19), induced by F_z for sinusoidal velocity. (a) The relative perturbation plotted for $(H_s - H)/H$ against H/L, with $\sigma_r = 0.1$. (b) The sensitivity of $|\overline{\delta}/\overline{v}|$ to σ_r at $\sigma_r = 0.1$, or $\partial(\overline{\delta}/\overline{v})/\partial\sigma_r$ (see text). Both have the common value $H'/H = 0.5$.

where $D_{1\text{-D}}$ is defined as $H(1 + \lambda_{1\text{-D}})$ for this geometry. The equivalent governing scale for this 2-D geometry now includes a dependence on L (via α).

[56] A second limiting case results from removing the sediment layer by letting $H_s \to H$ or $\sigma_r \to 0$. The numerator of the fraction in (15) becomes 0, and so $1 + \lambda_{2\text{-D}} \to 1$ as expected: there is no longer any shorting of the electric field through the sediment.

[57] A brief discussion of the F_h-induced perturbation component is presented here for completeness, but results from the cosine jet geometry are better suited for detailed analysis. The same reason applies as for why J_x induced by F_z is not realistic: adjacent regions of opposite velocity prevent the F_h-induced signal from decreasing to 0 as $H/L \to 0$.

[58] All of the signal induced by F_h is a perturbation from the 1-D approximation, so the depth-uniform perturbation is found by averaging the resulting E_x (denoted $E_{x,Fh}$) in the water column (not shown). In the small wave number limit this becomes

$$\lim_{\alpha \to 0} \overline{E}_{x,F_h} \to \frac{H'}{H} v_0 \sin(\alpha x) F_h \left(1 - \frac{H}{H_s}\right)\sigma_r. \qquad (17)$$

The magnitude of error at any x is independent of α, and so does not asymptotically approach the 1-D approximation. Nevertheless, its qualitative importance for small wave numbers is seen by the ratio of $\overline{E}_{x,F_h}/\overline{E}_{x,F_z}$

$$\frac{F_h}{F_z} \frac{\sin(\alpha x)}{\cos(\alpha x)} (1 - H/H_s)\sigma_r(1 + \lambda_{1\text{-D}}). \qquad (18)$$

This equation shows that $\overline{E}_{x,F_h}$ is out of phase with the velocity forcing and that it scales with F_h/F_z, σ_r, H/H_s, and $1 + \lambda_{1\text{-D}}$.

4.3. Parameter Space

[59] To analyze the four-dimensional parameter space we rely on the definitions in 3.1. The depth uniform perturbation is simplified by noting that $\lambda_{2\text{-D}}$ is uniform for all x. Dividing (7) by $\overline{v}$ gives the relative perturbation

$$\frac{\overline{\delta}}{\overline{v}} = 1 - \frac{1 + \lambda_{1\text{-D}}}{1 + \lambda_{2\text{-D}}}. \qquad (19)$$

Note that $(1 + \lambda_{1\text{-D}})/(1 + \lambda_{2\text{-D}})$ is always larger than 1. If, for instance, this fraction is 1.1, then the relative perturbation is 10%. Although equation (19) is always negative, the absolute value is shown in Figure 2a instead.

[60] There is a strong dependence of the depth-uniform relative perturbation $|\overline{\delta}/\overline{v}|$ on H/L and $(H_s - H)/H$ (Figure 2a). A transition point occurs at $H/L = 1$, below which the relative perturbation decreases exponentially with H/L, while above the relative perturbation is constant. The transition point makes sense by noting that the 1-D approximation requires a small vertical domain H relative to L to make $\mathbf{E}$ vertically uniform. Since electric fields tend to spread equally in all dimensions, thick sediments generate larger $\overline{\delta}$ because E_x does not penetrate evenly to the bottom of the sediment layer. The high wave number region $H/L > 1$ is not realistic, however, because geophysical ocean currents are always wider than they are deep.

[61] The sensitivity of the depth-uniform perturbation to σ_r is presented by $\partial(\overline{\delta}/\overline{v})/\partial\sigma_r$ (Figure 2b). This differential quantity is approximated by a centered difference, where the change in $\overline{\delta}/\overline{v}$ calculated for σ_r of $\sqrt{2}/10$ and $\sqrt{2}/20$ is simply divided by the twofold change in σ_r. For thin sediments (small $(H_s - H)/H$), $\lambda_{2\text{-D}}$ varies proportionally to σ_r, as expected from the 1-D definition of $\lambda_{1\text{-D}}$, but if the sediments are very thick the relative change is smaller. This demonstrates that if the electric field reaches fully to the bottom of the sediments then the sensitivity to σ_r is linear.

[62] Combining the dependence on $(H_s - H)/H$ and σ_r, both of which are linear in the lower left hand region of Figure 2, the perturbation turns out to be proportional to $\lambda_{1\text{-D}}$. This result is valid for sediment thinner than $(H_s - H)/H \leq 1$ and for aspect ratios less than $H/L \leq 0.5$.

5. Cosine Jet

[63] Although the sinusoidal geometry is analytically tractable, the solution does not asymptotically approach the 1-D approximation in the small wave number limit because of the infinite extent of the velocity field. A bounded velocity field is obtained by a finite Fourier summation of the sinusoidal solution for the cosine-jet velocity shown in Figure 1b. Similar approaches were used by *Longuet-Higgins et al.* [1954] and *Fristedt and Sigray* [2005], but

they solved for more restrictive geometries and did not seek general dependencies on the parameter space.

[64] The four nondimensional parameters are the same as in the sinusoidal velocity geometry, except now L refers to the full width of a bounded velocity field.

5.1. Solution Method

[65] The forcing is taken to be

$$v(x) = \begin{cases} \frac{1}{2}\left[1 + \cos\left(\frac{2\pi x}{L}\right)\right] & |x| < L/2 \\ 0 & |x| \geq L/2 \end{cases}, \quad (20)$$

because this form is symmetric about $x = 0$ and smoothly goes to 0 at $x = \pm L/2$ (Figure 1b).

[66] The solution becomes

$$\phi_i(x,z) = \sum_{n=0}^{N} a_{n,M}\left[A_i(z)\,\cos(k_{n,M}x) + B_i(z)\,\sin(k_{n,M}x)\right], \quad (21)$$

where $a_{n,M}$ is the Fourier coefficient for the (n, M)th wave number $k_{n,M} = 2\pi n/(M L)$, $n = 0, 1, 2, \ldots, N$, M is an integer $1 < M < N$ that determines the wave number resolution, and $A_i(z)$ and $B_i(z)$ are the depth-dependent coefficients for $\cos(\alpha x)$ and $\sin(\alpha x)$ for the regions $i = 1, 2, 3$ from (12). The coefficients $a_{n,M}$ are found by multiplying (20) by $\cos(k_{n,M}x)$ and integrating over $-\infty < x < \infty$ [Szuts, 2008].

[67] Although (21) is exact in the limit of $M, N \rightarrow \infty$, the fact that both of these constants are finite introduces two considerations for the solution. First, there is little loss of accuracy by terminating the summation at $N \gg M$, because the coefficients $a_{n,M}$ decay to 0 for $n \gg M$. Second, the value of M determines the repeat length of the solution, a fundamental property of finite Fourier expansions. The steep decrease in ϕ across the jet must be balanced by a gentle increase in potential outside of the jet for continuity of the cosine expansion at $x/L = \pm M$, which generates a nonzero electric field outside of the jet whose magnitude depends on M (see Appendix A).

[68] This background E_x is physically unrealistic and is removed as follows. A large value of M is chosen such that the background E_x is much smaller than $E_x(x = 0)$. An uniform E_x is added to the entire domain to obtain a zero background field and the result is scaled to maintain the initial maximum value of E_x. This procedure produces a valid solution because solutions to the Laplace equations are linear, and its accuracy is substantiated by the fact that the same final results are obtained for all values of M. The numerical dependence on M is discussed in greater detail in Appendix A, while the accuracy of the Fourier expansion technique is validated in Appendix B by comparison with the numerical Model for Ocean ElectroDynamics (MOED) [Tyler et al., 2004; also see SzII].

5.2. Representative Example

[69] The solution for one set of parameters is presented first to provide a physical basis for the 2-D solution and the velocity errors defined earlier. The example shown is for the largest aspect ratio ($H/L = 0.1$) that could be realistically expected, so that the 2-D perturbations are most obvious. The parameters used are width $L = 10$ km, jet depth $H' =$ 500 m, water depth $H = 1000$ m, sediment depth $H_s = 2000$ m, and relative sediment conductivity $\sigma_r = 0.1$.

5.2.1. Velocity Errors Induced by F_z

[70] The fields E_x and J_x induced by F_z are close to that expected from the 1-D approximation (Figures 3a and 3d). The horizontal electric field is not entirely vertically uniform, however, and there are negative but weak regions of E_x in the water column outside of the jet. The electric current density also varies slightly within each layer.

[71] The depth-uniform components and their perturbations are shown in Figure 3 (left). With $\lambda_{1\text{-D}} = 0.1$ for this geometry, $\bar{v}^*$ (dashed line, Figure 3b) is only 10% smaller than $\bar{v}$ (black line) and does not differ much from $\bar{v}_{1\text{-D}}^*$ (thick gray line). The depth-uniform velocity perturbation $\bar{\delta}$ from (7) (solid line, Figure 3c) has amplitudes of 0.002–0.004 m s^{-1} with a central maximum and minima close to $x = \pm L/2$ and spreads outside of the jet region. Even if this electric field outside the jet is incorrectly interpreted as due to a local velocity, the magnitude is less than 0.002 m s^{-1} (<2% relative to maximum $\bar{v}$). The magnitude of the depth-uniform error is summarized by ϵ (thick black line), which is 0.0025 m s^{-1}. The half width $L_{\bar{\delta}}$ is 0.04 L.

[72] If $\lambda_{1\text{-D}}$ can't be calculated for a particular observation location, it is possible to calculate an empirical λ if $\bar{v}$ is also known, denoted λ_{emp}. Either independent measurements of the absolute velocity can be made to find $\bar{v}$ [Larsen and Sanford, 1985], or else profiling instruments can be referenced to an absolute velocity [Nash et al., 2006]. At its simplest, the ratio $\bar{v}/\bar{v}^*$ should be equal to $1 + \lambda_{\text{emp}}$ according to the 1-D approximation. For greater statistical confidence, however, it is better to fit $1 + \lambda_{\text{emp}}$ to multiple observations of the variable velocity field [Spain and Sanford, 1987; Larsen, 1992].

[73] To apply this method to the cosine jet geometry, we assume that temporal changes in forcing (velocity) at one location can be described as horizontal meandering of the jet. With a flat bottom this is equivalent to sampling across a stationary jet. Thus, λ_{emp} is calculated by a horizontal average (denoted $< >_{\Delta x}$) over a horizontal range $x_0 - \Delta x < x < x_0 + \Delta x$ of

$$1 + \lambda_{\text{emp}} = < \bar{v}/\bar{v}^* >_{\Delta x}. \quad (22)$$

The value used for Δx is 100 m. The resulting depth-averaged perturbation analogous to (7) is

$$\bar{\delta}_{\text{emp}} = \bar{v} - \bar{v}^*(1 + \lambda_{\text{emp}}). \quad (23)$$

[74] The depth-uniform perturbation from λ_{emp} (dashed line, Figure 3c) is much smaller than that from $\lambda_{1\text{-D}}$ for this simple case. It is near zero in the center of the jet, with maximum values of 0.002 m s^{-1} in a small region near the edge of the jet.

[75] For comparison, the transport error from a submarine cable is also shown (dash-dotted line, Figure 3c). Submarine cables integrate the electric field on the seafloor across their length. The cable error is calculated as the difference between the horizontal integrals of $E_x(1 + \lambda_{1\text{-D}})/F_z$ and the exact quantity $v(x)$, normalized by the total transport of the jet and divided by 10 for display purposes. Despite a
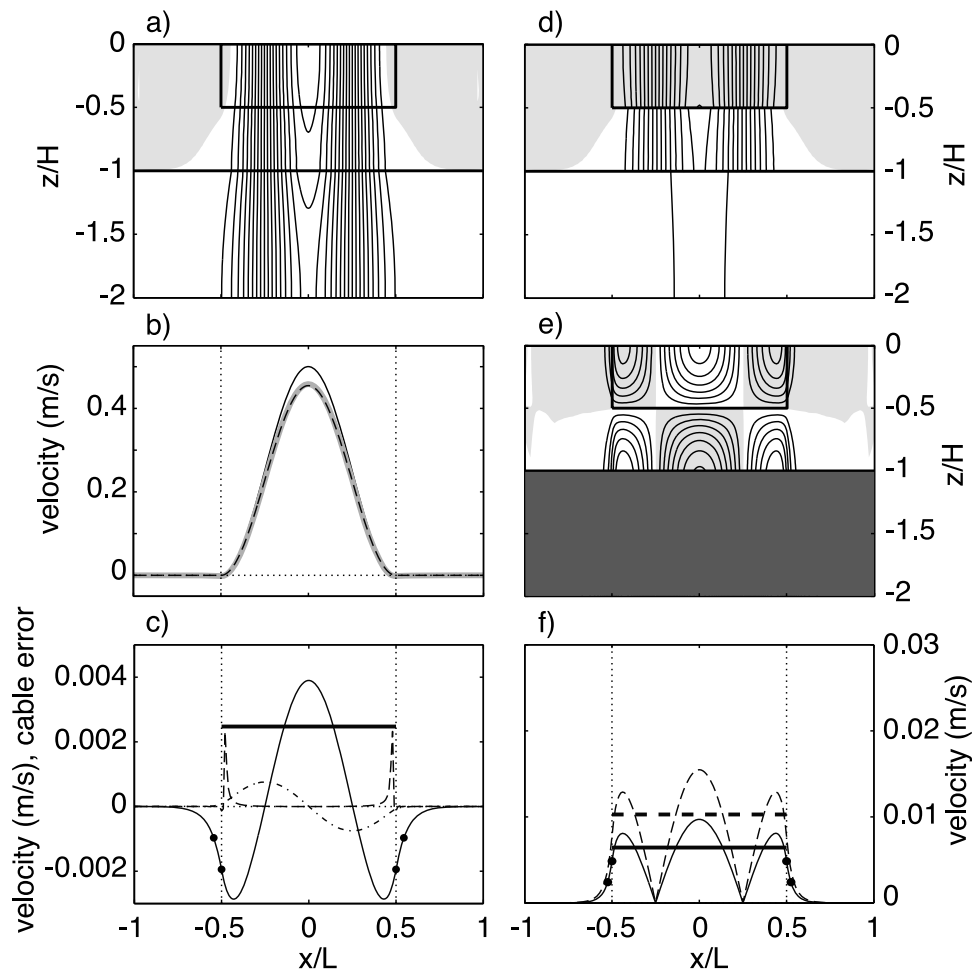
Figure 3. The solution induced by F_z for the cosine jet geometry with $H/L = 0.1$. The (left) depth-uniform and (right) depth-varying components are shown. (a) Electric field E_x, contours every 1 μV m^{-1}. (b) Depth-averaged velocity $\overline{v}$ (solid black), $\overline{v}^*_{\text{1-D}}$ (thick gray), and $\overline{v}^*$ (dashed black). (c) Velocity perturbation $\overline{\delta}$ (thin solid) and error ϵ (thick solid), empirical depth-uniform velocity perturbations $\overline{\delta}_{\text{emp}}$ (dashed), and the cable error divided by 10 (see text, dash-dotted). (d) Electric current density J_x, contours every 1 μA m^{-2}. (e) Depth-varying perturbation δ', contours every 0.002 m s^{-1}. (f) For the depth-varying perturbations δ'_{std} (solid) and the biased perturbations (dashed), the vertical second moment $\delta'_{\text{std}}(x)$ (thin) and depth-varying error ϵ' (thick). Dots in Figures 3c and 3f show the end points of the half-width decay length. The solution is for a small width jet defined by $L = 10$ km, $H' = 500$ m, $H = 1000$ m, $H_s = 2000$ m, and $\sigma_r = 0.1$. The boxes in Figures 3a, 3d, and 3e delineate where velocity is nonzero.

maximum error of 0.8%, there is no error if the cable spans either half of the jet because of symmetry.

[76] The other type of perturbation is depth varying, shown in Figure 3 (right). In the water column, the depth-varying perturbations (Figure 3d) are surface and bottom intensified. The vertical second moment δ'_{std} is at most 0.01 m s^{-1} (thin black line, Figure 3e), with an RMS value ϵ' of 0.0065 m s^{-1} (thick black line). The bias introduced by referencing the relative velocity profile near the surface results in 60% larger perturbations.

5.2.2. Velocity Errors Induced by F_h

[77] The 1-D approximation only accounts for signals induced by F_z, so any signal from F_h is considered a perturbation in full. With the bounded velocity of the cosine jet, the perturbations induced by F_h decay to 0 as the aspect

ratio decreases, in agreement with the expectation from the 1-D approximation.

[78] These calculations assume that the ocean velocity flows towards magnetic east, and thus that the F_h-induced signal is maximum. Flows with no magnetic east component generate no F_h-induced signal, and more generally the magnitude depends on $\sin(\theta)$, where θ is the heading in magnetic coordinates (clockwise from 0 at magnetic north).

[79] The velocity perturbations defined earlier need to be modified slightly for the F_h-induced components. The quantities F_z and $\lambda_{\text{1-D}}$ are used for normalizing to obtain velocity, because any perturbations induced by F_h will be initially indistinguishable from the first-order signal. The velocity perturbations will thus also depend linearly on F_h/F_z and be larger near the magnetic equator and smaller near the poles.
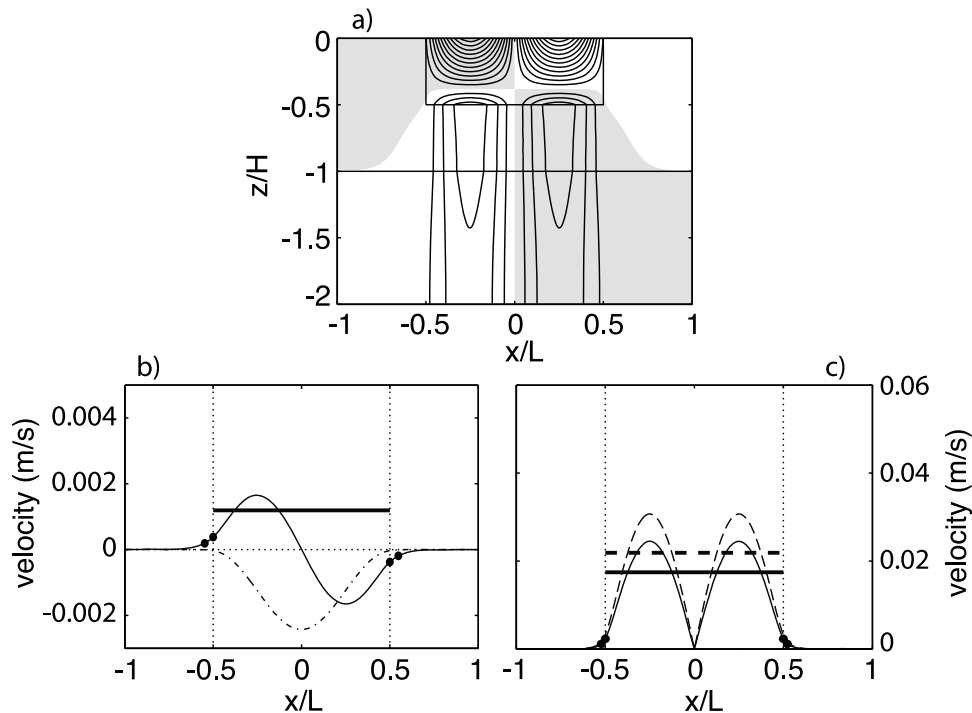
Figure 4. The solution induced by F_h for the cosine jet geometry with $H/L = 0.1$, if they are interpreted as generated by F_z (see text). (a) The depth-varying velocity perturbation δ'_{F_h}, contours every 0.005 m s^{-1}. (b) The depth-uniform velocity perturbation $\overline{\delta}_{F_h}$ (thin), ϵ (thick), the location of the half widths on either side of the jet (dots), and the cable error (see text, dash-dotted). (c) The depth-varying perturbation, same as Figure 3f. Aside from $F_h/F_z = 0.5$, the other parameters are the same as in Figure 3.

[80] The velocity perturbations defined by (7), (8) and (11) are modified by removing the expected velocities $\overline{v}$ and $v(x, z)$ from the equations, giving the modified forms

$$\overline{\delta}_{\lambda_{1-D,F_h}} = \overline{v}^*_{F_h}(1 + \lambda_{1-D}) \tag{24}$$

$$\delta'_{F_h}(x,z) = \frac{J_x(x,z)}{\sigma(z)F_z} - \overline{\delta}'_{F_h}(x)$$

$$\overline{\delta}'_{F_h}(x) = \frac{1}{H}\int_{-H}^{0}\left[\frac{J_x(x,z)}{\sigma F_z}\right]dz. \tag{25}$$

The definitions of the biased quantities $\delta'_{\text{bias},F_h}$ and $\overline{\delta}_{\text{bias},F_h}$ are obvious by comparison with the above. The quantity λ has no physical meaning for the contribution from F_h because $\lambda_{1-D,F_h} = 0$, so (22) and (23) are not calculated.

[81] The perturbations induced by F_h are most important near edges of the velocity jet (Figure 4), which is also where the relative perturbation is largest because the dominant signal induced by F_z decays to zero. The RMS depth-uniform quantity $\overline{\epsilon}_{F_h}$ is 0.0012 m s^{-1}, the same order of magnitude but slightly smaller than that generated by F_z. The cable transport error, now the integrated and scaled electric field divided by the maximum jet transport (still scaled by 0.1 for display purposes), is small compared with the total transport (2.4%) and still integrates to 0 if the cable fully spans the jet.

[82] The depth-varying velocity error ϵ' is 0.019 cm s^{-1}, roughly 2 times larger than that induced by F_z. The biased perturbations are only 25% larger than δ'_{std} and ϵ'. The half widths are similar to those induced by F_z.

5.3. Parameter Space

[83] Having described the 2-D perturbations for one set of parameters, now we present the dependence of these velocity errors (in m s^{-1}) or half widths (normalized by D_{1-D}) on the nondimensional parameters (Figures 5 and 6). Based on the realistic range of H/L discussed in section 6, the discussion focuses on $H/L \leq 10^{-0.5}$ even though a wider range is shown for completeness.

[84] The shape of lines of constant error ϵ (Figure 5a) are similar to the sinusoidal velocity forcing (Figure 2a) but do not have as sharp a transition between the small and large regimes of H/L. A weaker transition region remains at H/L of 0.5–1, below which the depth-uniform velocity error decreases exponentially with H/L and $(H_s - H)/H$. The dependence on σ_r is close to linear for $(H_s - H)/H < 1$ (not shown), in agreement with the results for the sinusoidal geometry. Combining the dependence on $(H_s - H)/H$ and σ_r, for sediment as thick as the water column the error is <0.01 m s^{-1} if $H/L \leq 0.01$ $\lambda_{1-D}^{-5/2}$ (approximating the 10^{-2} contour).

[85] The depth-uniform error can also be quantified for a cable, with the understanding that any cable that spans either half of the velocity jet will have a net error of zero. The maximum cable error within $-L/2 < x < L/2$ (not shown) is independent of sediment thickness for $(H_s - H)/H < 1$ and is roughly 100 times smaller than Figure 5b, while for thicker sediments the maximum cable error increases
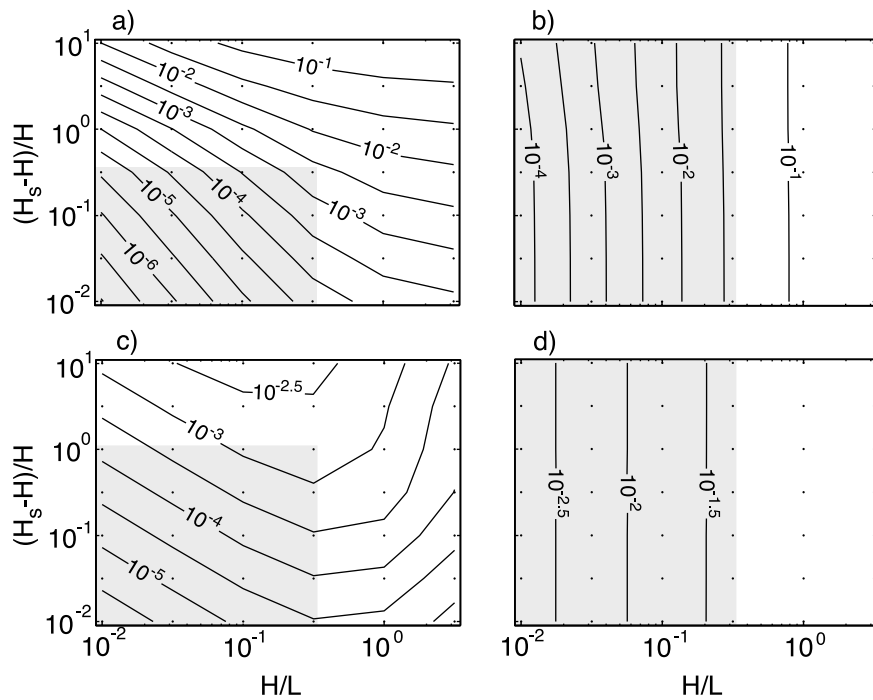
Figure 5. (left) Depth-uniform and (right) depth-varying velocity errors for the cosine jet geometry induced (top) by F_z and (bottom) by F_h: (a) ϵ (m s^{-1}), (b) ϵ' (m s^{-1}), (c) ϵ_{F_h} (m s^{-1}), and (d) ϵ'_{F_h} (m s^{-1}). The remaining parameters are $H'/H = 0.5$ and $\sigma_r = 0.1$. Dots indicate where solutions are calculated, and shading indicates the region over which the error is fit (see Table 1).
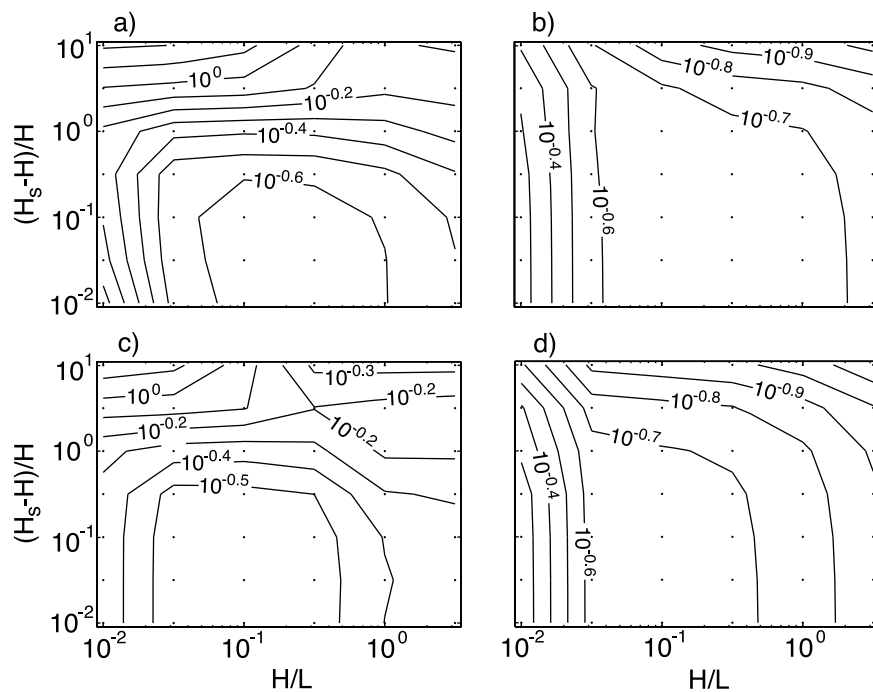
Figure 6. Half widths normalized by $D_{1\text{-D}}$ of (left) depth-uniform and (right) depth-varying perturbations induced by (top) F_z and by (bottom) F_h: (a) $L_{\bar{\delta}}/D_{1\text{-D}}$, (b) $L_{\delta'}/D_{1\text{-D}}$, (c) $L_{\bar{\delta},F_h}/D_{1\text{-D}}$, and (d) $L_{\delta',F_h}/D_{1\text{-D}}$. The remaining parameters are the same as in Figure 5.

Table 1. Fits of the Velocity Errors ϵ or ϵ' to (26) Over the Regions in Figure 5 Indicated by Gray Shading and for $H'/H = \{0.25, 0.5, 0.75\}$ and $\sigma_r = \{0.05, 0.1, 0.2\}$[a]

Error	F	a	b	c	d	e	Relative RMS Error
ϵ	F_z	1.87	1.09	0.44	1.02	0.87	0.17
ϵ	F_h	0.86	0.97	2.03	1.00	0.31	0.13
ϵ'	F_z	1.83	0.050	0.15	0.08	0.44	0.17
ϵ'	F_h	0.94	−0.0006	1.19	−0.0014	0.31	0.06

[a]The relative RMS error of the fit is calculated as RMS($\epsilon/\epsilon_{fit} - 1$). The coefficients are precise to ±0.01, a−d are dimensionless, e has dimensions of velocity, and all fits have $R^2 \geq 0.993$.

strongly with $(H_s - H)/H$, similar to the part of Figure 5a for $(H_s - H)/H > 1$.

[86] The depth-varying velocity error ϵ' (Figure 5b) has no dependence on the sediment thickness, and the magnitude of the error decreases exponentially with H/L for $H/L < 0.5$. The error is <0.01 m s^{-1} if $H/L \leq 0.2$. The dependence on σ_r is very weak.

[87] A factor 5 change in H' (from $H'/H = 0.5$ to 0.1) reduces the depth-uniform and depth-varying errors by factors of 3–5, where the larger reduction occurs for thick sediment and large H/L (not shown). These reductions can be generalized by a linear (or slightly less than linear) dependence of both errors on $\bar{v} = v_0 H'/H$.

[88] The depth-uniform errors induced by F_h are generally smaller than those induced by F_z and depend mostly on the sediment thickness (Figure 5c). For any aspect ratio, errors are below 0.003 m s^{-1} if the sediment is less than 3 times as thick as the water column. By contrast, the depth-varying errors due to F_h (Figure 5d) are larger than those due to F_z: an error <0.01 m s^{-1} occurs if $H/L \leq 0.06$. The transition region to uniform error ϵ' with H/L still occurs at $H/L = 0.5$.

[89] The influence of H' is much stronger for the F_h contribution (not shown): if H'/H changes from 0.5 to 0.1, the depth-uniform error is reduced by 2–10, while the depth-varying error is reduced by 25–30.

[90] Over the lower left corner of the parameter spaces indicated by gray shading in Figure 5, the errors ϵ and ϵ' can be summarized by the functional form of (Table 1)

$$\left(\frac{H}{L}\right)^a \left(\frac{H_s - H}{H}\right)^b \left(\frac{H'}{H}\right)^c (\sigma_r)^d e. \quad (26)$$

The large R^2 values (>0.993) indicate a highly accurate fit, and the RMS fractional residual is less than 20%. The errors induced by F_z (F_h) depend on H/L to the power of 1.85 (0.90). The depth-uniform errors depend nearly proportionally to the sediment thickness and sediment conductivity (powers of 1) and on the jet depth to the power of 0.5; whereas the depth-varying errors have few other dependencies. Note that the depth-uniform error induced by F_z has a larger dependence on sediment thickness if $(H_s - H)/H > 1$. The jet depth influences the depth-uniform error induced by F_z slightly (powers less than 0.4) as well as stronger dependencies for the depth-uniform (power 2) and depth-varying (power 1.2) errors induced by F_h.

[91] The decay half widths outside of the forcing region are shown in Figure 6, where normalization by $D_{1\text{-D}}$ corrects for the 1-D effect of sediment thickness. The ratio plotted is

the scale factor for $D_{1\text{-D}}$ that describes an effective horizontal averaging distance. That the values are almost identical for perturbations induced by F_z or by F_h confirms that the passive response of the geometry is independent of the forcing (for this set of H' and σ_r). For $L_{\bar{\delta}}$, the half width has a lower limit of 0.3 $D_{1\text{-D}}$ ($10^{-0.5}$) at $H/L = 0.1$ for moderately thin sediment ($(H_s - H)/H < 10^{-0.5}$) and it increases proportionally with sediment thickness and inversely with H/L. Although depth-varying errors have slightly smaller half widths for the same aspect ratio, $L_{\delta'}$ is relatively unaffected by sediment thickness if $H/L < 0.1$. The parameter space does not suggest that an asymptotic value of $L_{\bar{\delta}}$ or $L_{\delta'}$ is reached for very small H/L, with maximum values of 0.5–1.2 $D_{1\text{-D}}$ obtained at the smallest resolved H/L.

6. Discussion

[92] Overall, this study aims to address the relative importance of 2-D perturbations in motionally induced signals that arise in the presence of velocity gradients. Our approach isolates the 2-D errors in calculating velocity from E and J on the basis of nondimensional scales. Additional context is necessary for understanding the physical implications of these results and their extension to different situations.

[93] Specifically, before the results are generalized two matters need to be discussed: the nondimensional parameters were prescribed without recourse to geophysical constraints, so it remains to proscribe the regions of parameter space that are unrealistic; and the shape of the two geometries was reductionist by necessity, thus salient features are discussed as a guide for extrapolating our results to different geometries.

[94] The previous two points provide a basis for generalizing the results. First a physical explanation of 2-D perturbations is presented. Then, over the realistic region of the parameter space previously defined, we specify the sensitivity of 2-D perturbations to geometrical and electrical parameters as well as their magnitudes.

[95] Broader discussion of these results and their application to one study site is presented in SzII, where the addition of 2-D perturbations caused by sloping topography is needed for a more complete discussion.

6.1. Constraints on Aspect Ratio and Other Parameters

[96] The schematic geometries were chosen to facilitate a parameter-space analysis and were not constrained to be realistic a priori. Fluid dynamics theory and observed oceanic flows provide a sense of the maximum aspect ratios possible.

[97] In the open ocean, geostrophic balance is the primary dynamic equilibrium. Flow adjusts to geostrophy within a distance of the Rossby radius, whether for barotropic responses ($R_{BT} = \sqrt{gH}/|f|$) or for baroclinic responses ($R_{BC} = c_n/|f|$, where c_n is the wave speed of the nth baroclinic mode). The definitions of barotropic and baroclinic velocities used here are depth-averaged and depth-varying velocities, respectively. Even at high latitudes and in shallow water the barotropic Rossby radius is greater than 200 km (for $H \geq 100$ m, all latitudes), such that $H/R_{BT} \leq 0.005$ and the 1-D approximation is appropriate; while the baroclinic Rossby radius is 10–30 km at high latitudes and

increases towards the equator [Gill, 1982], such that H/R_{BC} can potentially reach 0.1 at high latitudes.

[98] A second way to consider baroclinic aspect ratios is with the Burger number $S^{1/2} = N H/(f L)$, the ratio of H/L to the eccentricity of ellipse f/N described by geostrophic motion. The value of S is typically less than 1, which, for typical stratification ($N \leq 0.003$ s^{-1}) and latitudes equatorward of 60°, implies that H/L is less than 0.003. For a given Burger number, the width L is set by the forcing: a baroclinic response occurs if the water depth is shallower than $f L S^{1/2}/N$, otherwise the response is barotropic with a smaller aspect ratio ($H/L < f S^{1/2}/N$).

[99] A brief survey of fine-scale processes and locations is in agreement with the general theoretical constraints mentioned above: equatorial internal waves ($H/L = 0.1$ [Lien et al., 2002]), internal solitons ($H/L = 0.1$ [Chang et al., 2008]), coastal currents (California Current $H/L = 0.005$, California Undercurrent $H/L = 0.025$ [Hickey, 1979]), headland eddies ($H/L = 0.02$ [Pawlak et al., 2003]), and eddies along a shelf break front ($H/L = 0.01$ [Churchill and Gawarkiewicz, 2009]).

[100] Hydraulic constraints lead to different dynamic scalings, such as flow through sills in which the velocity jet is bottom trapped and constrained by topography. Considering the barotropic component to be set by the sill cross section, the aspect ratios of depth to width have a maximum of 0.03 for a number of examples (0.012 for the Denmark Strait [Girton et al., 2001], 0.01–0.02 for the Strait of Gibraltar [Baringer and Price, 1997], 0.0003–0.007 for Indonesian sills [Hautala et al., 2001], or 0.03 for the Windward Passages [Wilson and Johns, 1997]).

[101] This limited discussion suggests an upper limit for H/L of 0.03 for barotropic flows and 0.1 for baroclinic flows. Ultimately, the wide disparity between the definition of nondimensional parameters in our geometry compared to analytical theory prevent more than a qualitative comparison of the two.

[102] The ranges of other parameters are limited in more obvious fashions. The depth of the moving surface layer clearly occupies values $0 < H'/H \leq 1$ and cannot be further constrained. Sediment thickness and relative sediment conductivity have ranges of 0–10 km and 0.02–0.5 and are discussed in more detail in SzII.

6.2. Limitations of Resolved Geometries

[103] Both geometries investigated contain surface intensified oceanic flow that has depth-averaged and depth-varying components. Although these geometries were chosen to be broadly applicable, there are four limitations to note for applying our results to other situations and geometries.

[104] 1. The cosine jet geometry is an idealized cross section, and the side boundaries of velocity can be sharper or the central region of large transport can be wider. Both changes would generate larger 2-D perturbations at the edges than the cosine jet. It is not just the local velocity gradient that is important, but the spatial distribution of nearby velocity.

[105] 2. The two layer ocean flow describes a vertical step change in velocity. This sharp boundary maximizes the vertical second moment of velocity error. Smoother vertical structure will generate smaller depth-varying errors.

[106] 3. The choice of uniform conductivity in the ocean layers ignores salinity stratification. The small range of conductivity in the open ocean leads to a small distortion that is corrected with the factor γ (<10% affect for open ocean modes [Chave and Luther, 1990]). Further investigation of this correction procedure is needed in regions with extreme salinity contrasts, especially if the geometry can lead to 2-D perturbations.

[107] 4. All geometries have a barotropic velocity, so care needs to be taken when extending these results to the predominantly baroclinic flow often measured with profiling floats. In particular, this analysis can't distinguish the relative contributions of the barotropic and baroclinic velocity forcing to the depth-varying perturbations. The aspect ratio of baroclinic flows is expected to remain a key parameter to describe 2-D perturbations for internal waves or modes. It is difficult to generalize the aspect ratios of baroclinic features, because internal modes or waves have small vertical structure, propagate at an angle in the vertical, and have a wide range of horizontal coherence (whether a mode or beam). Length scales in both horizontal directions must be considered. The analytical study of Preisendorfer et al. [1974] discusses baroclinic velocity modes based on infinite sinusoidal forcing, similar to the sinusoidal velocity geometry presented here. From this similarity, we expect that the deficiency of our analytic solution is also apparent in theirs, namely that electric currents do not asymptotically approach the 1-D approximation as the aspect ratio decreases. Further study is needed to more accurately resolve the depth-varying velocity errors associated with high-mode baroclinic flow.

6.3. Physical Meaning, Sensitivity, and Magnitude of 2-D Perturbations

[108] The example shown in Figure 3 uses an aspect ratio at the upper limit of what is realistic. To illustrate the 2-D perturbations in general, however, unrealistically narrow width scales are necessary to accentuate the changes. The perturbations induced by F_z are illustrated in Figure 7 with an electric current stream function ψ (Figure 7, top, defined as $\nabla \times \hat{\jmath} \, \psi = \mathbf{J}$) and by the electric potential ϕ (Figure 7, bottom). The stream function is calculated directly with the same Fourier summation used to calculate $\mathbf{E}$ and $\mathbf{J}$.

[109] When the velocity aspect ratio is very small, a nearly 1-D solution, vertical isopotentials (Figure 7c) show that electric currents (Figure 7a) are confined within the jet and are nearly horizontal. With a large aspect ratio, these currents have a significant vertical component and no longer fully reach the bottom of the sediment column (Figure 7b). The electric field is weaker in the sediment and is no longer vertically uniform (Figure 7d). When the aspect ratio increases the thin layer approximation breaks down, and, because $\mathbf{E}$ and $\mathbf{J}$ spread isotropically, nonnegligible circuits form in the vertical.

[110] The parameter space analyses show that there is a common transition point in the velocity errors at H/L of 0.5–1, which fortuitously coincides with the realistic range of H/L for both depth-averaged ($\lesssim 0.03$) and depth-varying ($\lesssim 0.1$) flows. This feature allows the errors to be described as powers of the nondimensional parameters, which aids in determining the sensitivity of errors as well as predicting their magnitude.
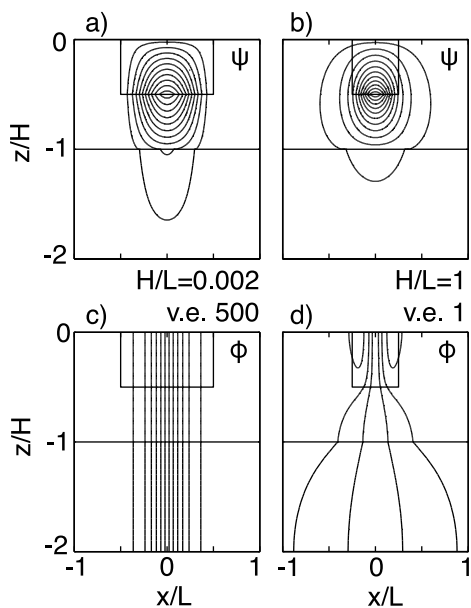
Figure 7. The 2-D perturbations in (top) the electric current stream function ψ and (bottom) the electric potential ϕ induced by F_z for small and large aspect ratios with the cosine jet geometry. (left) A nearly 1-D response (H/L = 0.002, vertical exaggeration of 500) contrasts with (right) a strongly 2-D response (H/L = 1, no vertical exaggeration). Contour spacings are (a) 0.004 A m^{-1}, (b) 0.002 A m^{-1}, (c) 0.4 V, and (d) 0.002 V. Unspecified nondimensional parameters are the same as in Figure 5 from SzII, which describes sloping topography.

[111] Although independent of the magnitude of the errors, their sensitivity to the nondimensional parameters is a more robust result given that it better reflects the underlying magnetostatic response independent of the specific geometry. Perturbations induced by F_z (F_h) depend on H/L to the power of 1.9 (0.9), which provides a more specific relationship than the order of magnitude H/L scaling described in the perturbation analysis of *Sanford* [1971]. This dependence on H/L holds and is uniform over its realistic range (H/L < 0.5). Depth-uniform errors depend on the sediment thickness and conductivity to the power of one, which means their combined dependence is proportional to $\lambda_{1\text{-D}}$. On the other hand, depth-varying errors are nearly independent of sediment thickness and conductivity. Lastly, the depth of the jet has little impact on the perturbations induced by F_z (powers of 0.15–0.5), whereas they have stronger influences on perturbations induced by F_h (powers or 1–2).

[112] For the same aspect ratio (H/L = 0.1), depth-varying errors generated by velocity gradients and F_h are larger (0.015 m s^{-1}) than those generated by F_z (0.003 m s^{-1}). Because the relative magnitude of errors induced by F_z and F_h depends on the ratio F_z/F_h, set here to represent midlatitudes, the relative importance changes with geomagnetic latitude. Although the 1-D approximation breaks down at the geomagnetic equator (where F_z = 0), there have been successful measurements with profiling instruments up to 2°

in latitude from the geomagnetic equator [*Kennelly et al.*, 1986].

[113] The effective horizontal averaging distance is found to be 0.2–1.2 $D_{1\text{-D}}$. The half widths do not approach an upper asymptote at the lowest resolved values of H/L, as might be expected for a 1-D asymptote. This merely reflects the dominance of the forcing width scale at small aspect ratios, for which the small magnitude perturbations (<0.1%) are of little importance. Our results are consistent with *Chave and Luther* [1990], who found that EF solutions are averaged over a radius a "couple times the water depth" in their flat-bottomed ocean with $H/L \ll 1$, with the specification that $D_{1\text{-D}}$ is the vertical scale that best describes the motionally induced response.

7. Conclusion

[114] In regions where there are strong horizontal velocity gradients, there can be 2-D perturbations on top of the dominant 1-D motionally induced signals. This article addresses the extent to which these perturbations depend on the surrounding geometrical and electrical nondimensional parameters. More specifically, we characterize the magnitude and sensitivity of 2-D perturbations generated by velocity gradients. The parameter with the greatest influence on 2-D perturbations is the aspect ratio of the oceanic flow, but there are additional contributions from the remaining parameters of sediment thickness, sediment conductivity, and the thickness of the oceanic flow.

[115] For typical values of the nondimensional parameters, the maximum errors introduced by a 1-D interpretation of the 2-D solution are no larger than a few percent. Over the realistic range of the parameter space (aspect ratios smaller than 0.1, sediments thinner than 10 times the water depth, and sediments on average 10 times less conductive than seawater) the simple shape of the 2-D velocity errors enables their sensitivity to the nondimensional parameters to be readily calculated. The depth-uniform and depth-varying velocity errors depend on the aspect ratio to the power of 1.9 (induced by F_z) or 1 (induced by F_h). Depth-uniform errors are linearly proportional to $\lambda_{1\text{-D}}$, which includes both sediment thickness and sediment conductivity. Depth-varying errors, by contrast, have minimal dependence on either sediment thickness or sediment conductivity. The jet depth has a stronger influence on signals induced by F_h (powers of 1–2) and a weaker influence on signals induced by F_z (powers of 0.2–0.4).

[116] In both geometries, the velocity error decays outward from the forcing over a half width of 0.2–1 $D_{1\text{-D}}$, the effective water depth from the 1-D approximation. This result suggests that $D_{1\text{-D}}/L$ is a more accurate assessment than H/L of whether a given situation contains 2-D effects in the depth-uniform component. In contrast, because depth-varying errors are insensitive to sediment properties, the depth-varying errors are governed by H/L.

[117] This analysis has sought general results that are applicable to many types of oceanic electromagnetic measurements and that allow estimates of the magnitude of 2-D perturbations generated by velocity gradients. Further discussion is given after the role of sloping topography is quantified in SzII. The expected errors generated by velocity
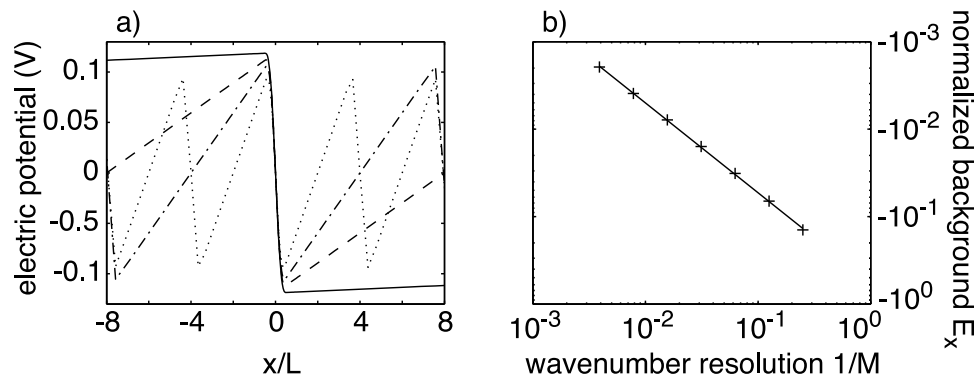
Figure A1. (a) The electric potential ϕ at $z = -H'/H$ for $M = 4$ (dotted), $M = 8$ (dash-dotted), $M = 16$ (dashed), and $M = 256$ (solid). For lower values of M the domain is small enough to show that the solution has a period $M\,x/L$. (b) The normalized background E_x ($\overline{E}_x/\max(\overline{E}_x)$) plotted against the wave number resolution $1/M$. In logspace, the slope of the best-fit line is -1.028 ± 0.007. The parameter set used is $H = 3000$ m, $H' = 500$ m, $H_s = 6000$ m, $L = 100$ km, and $\sigma_s/\sigma = 0.4$.

gradients, however, are both small and sensitive to the geometric parameters in a simple fashion, which confirms the accuracy of measurements based on motional induction.

Appendix A: Convergence of Finite Velocity Numerical Evaluation

[118] A numerical difficulty with the discrete and finite Fourier cosine expansion used in section 5 is the presence of a nonzero but uniform background E_x. By varying the value of M for one set of parameters (Figure A1), it is clear that the background E_x scales as M^{-1}. This result is confirmed analytically by *Szuts* [2008]: to first order, the finite Fourier expansion is in error from the exact continuous equivalent by $M^{-1}/2 - M^{-2}/6$.

[119] There are two ways to minimize the influence of this numerical issue: choose a very large M (>100), or subtract a uniform E_x from the solution and scale the result. The former was at the expense of computation time and was too prohibitive if solutions over a wide parameter space are

desired. The latter choice is physically sound, since solutions of the Laplace equations are linearly independent. With this choice, M is chosen to make the offset in E_x outside of the jet much smaller than the forcing amplitude at $x = 0$. Adjusted solutions thus obtained are independent of M and are close to the asymptotic solution for very large M [*Szuts*, 2008].

[120] In practice, the value of M depends on H/L. For large values of H/L the electric field spreads horizontally far outside of the jet. The repeating nature of the Fourier expansion thus requires a larger repeat length (larger M) to properly resolve the uniform offset in E_x. This is implemented first by defining an heuristic distance at which E_x becomes uniform as

$$M_h = 12\Big(H + (H_s - H)\frac{\sigma_s}{\sigma}\Big)/L + 1 = 12 D_{1\text{-D}}/L + 1.$$

This formulation stresses that $D_{1\text{-D}}$ is the key vertical scale for the magnetostatic response. The value of M used is the
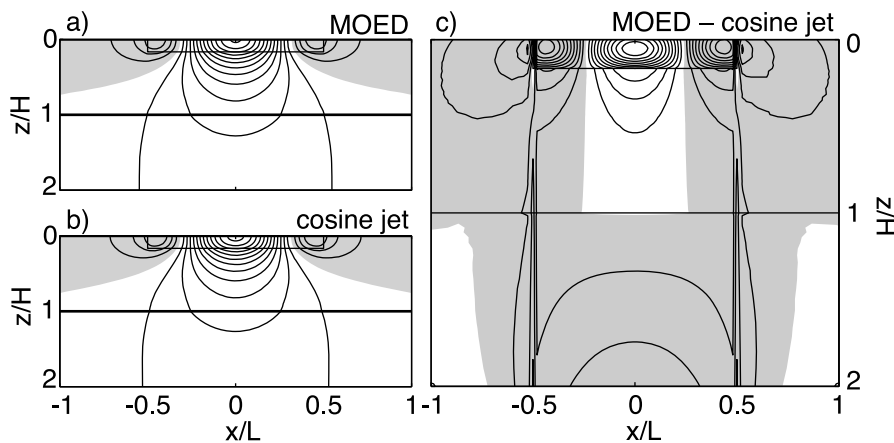
Figure B1. Comparison of Fourier summation of analytic results with MOED output for E_x. (a) E_x from MOED. (b) E_x for the cosine jet geometry with Fourier expansion. For both, the parameters that define the geometry are $L = 5$ km, $H' = 500$ m, $H = 3000$ m, $H_s = 6000$ m, and $\sigma_r = 0.4$, and contours of E_x are every 1 μV m^{-1}. (c) The difference between Figures B1a and B1b gridded to the MOED grid, with contours every 0.02 μV m^{-1}. Negative regions are shaded gray.

second higher power of two. A minimum value of 8 is used for small M_h, while the maximum used is 128 to keep computation times reasonable.

Appendix B: Cross Validation of the Analytic Solution and MOED

[121] To cross validate the Fourier-expanded cosine jet technique (section 5.1) and the MOED model (section 4 in SzII), solutions for the same geometry are compared here.

[122] The different numerical techniques give rise to slight differences in the output. The analytic solution is calculated exactly at every location, with any error from the true solution resulting from the truncated and finite Fourier summation. The accuracy of the numerical model, however, depends on how well the grid resolves the step changes in conductivity structure. Much care is needed in setting the resolution and the grid over a large parameter space.

[123] The discrete nature of a grid also introduces a difference between the desired geometry and that resolved by the model. For instance, the vertical step change in velocity at $z = -H'$ is interpreted by the model as a linear change between two vertical grid points. Similarly, the vertically integrated conductivity or velocity are discrete approximations that lead to small differences in $\bar{v}$ and $\lambda_{1\text{-D}}$ in relation to the analytical solution. The MOED solution is scaled by $1/1.09$ to correct for solutions that are 9% larger than in the cosine jet solution.

[124] The horizontal and vertical grid spacings used in MOED are $\Delta x = 10$ m and $\Delta z = 5$ m in the jet, with Δz slowly increasing outside of the forcing region. In the cosine jet solution, the z grid is resolved within $\epsilon = \pm 5 \times 10^{-8}$ m of $z = -H'$ and $z = -H$ to allow for more accurate vertical integrals of the resulting output.

[125] A small L and a small H' are chosen for this comparison so that the situation is fully 2-D. The two techniques agree very well for E_x (Figure B1) and E_z (not shown). The difference between the solutions (Figure B1c) is an order of magnitude smaller than the solution itself. The maximum magnitude of E_x is 12.4 μV m^{-1}, and the maximum, mean, and second moments of the difference between the solutions over the region $-1/2 \leq x/L \leq 1/2$ and $-H_s \leq z \leq 0$ are 0.11 μV m^{-1} (relative error of 0.9%), 0.012 μV m^{-1} (0.1%), and 0.05 μV m^{-1} (0.4%). The maximum magnitude of E_z is 7.5 μV m^{-1}, and the maximum, mean, and second moments of their difference over the same region are 0.66 μV m^{-1} (9%), 0.0000014 μV m^{-1} (0.0002%), and 0.09 μV m^{-1} (1.2%).

References

Baringer, M. O., and J. C. Larsen (2001), Sixteen years of Florida Current transport at 27°N, *Geophys. Res. Lett.*, *28*, 3179–3182.

Baringer, M. O., and J. F. Price (1997), Mixing and spreading of the Mediterranean outflow, *J. Phys. Oceanogr.*, *27*, 1654–1677.

Chang, M.-H., R.-C. Lien, T. Y. Tang, Y. J. Yang, and J. Wang (2008), A composite view of surface signatures and interior properties of nonlinear internal waves: Observations and applications, *J. Atmos. Oceanic Technol.*, *25*, 1218–1227.

Chave, A. D., and D. S. Luther (1990), Low-frequency, motionally induced electromagnetic fields in the ocean: 1. Theory, *J. Geophys. Res.*, *95*(C5), 7185–7200.

Chave, A. D., D. S. Luther, and J. H. Filloux (1992), The Barotropic Electromagnetic and Pressure Experiment: 1. Barotropic current response to atmospheric forcing, *J. Geophys. Res.*, *97*(C6), 9565–9593.

Churchill, J. H., and G. G. Gawarkiewicz (2009), Shelfbreak Frontal eddies over the continental slope north of Cape Hatteras, *J. Geophys. Res.*, *114*, C02017, doi:10.1029/2007JC004642.

Cunningham, S. A., et al. (2007), Temporal variability of the Atlantic meridional overturning circulation at 26.5°N, *Science*, *317*(5840), 935–938, doi:10.1126/science.1141304.

Flosadóttir, Á. H., J. C. Larsen, and J. T. Smith (1997), Motional induction in North Atlantic circulation models, *J. Geophys. Res.*, *102*(C5), 10,353–10,372.

Fristedt, T., and P. Sigray (2005), The motionally induced electric field from a two-layer channel-flow of rectangular or ellliptical cross-section: A possibility to resolve baroclinic flow features?, technical report, Dep. of Meteorol. Phys. Oceanogr., Univ. of Stockholm, Stockholm.

Gill, A. E. (1982), *Atmosphere-Ocean Dynamics*, *Int. Geophys. Ser.*, vol. 30, 666 pp., Academic, San Diego, Calif.

Girton, J. B., T. B. Sanford, and R. H. Käse (2001), Synoptic sections of the Denmark Strait Overflow, *Geophys. Res. Lett.*, *28*(8), 1619–1622.

Hautala, S. L., J. Sprintall, J. T. Potemra, C. C. Jackson, W. Pandoe, N. Bray, and A. G. Ilahude (2001), Velocity structure and transport of the Indonesian Throughflow in the major straits restricting flow into the Indian Ocean, *J. Geophys. Res.*, *106*(C9), 19,527–19,546.

Hickey, B. M. (1979), The California current system—Hypotheses and facts, *Progr. Oceanogr.*, *8*(4), 191–279.

Kennelly, M. A., P. A. McKeown, and T. B. Sanford (1986), XCP performance near the geomagnetic equator, *Tech. Rep. 8607*, Appl. Phys. Lab., Univ. of Wash., Seattle, Wash.

Larsen, J. C. (1968), Electric and magnetic fields induced by deep sea tides, *Geophys. J. Int.*, *16*, 40–70.

Larsen, J. C. (1971), The electromagnetic field of long and intermediate water waves, *J. Mar. Res.*, *29*(1), 28–45.

Larsen, J. C. (1992), Transport and heat flux of the Florida Current at 27°N derived from cross-stream voltages and profiling data: Theory and observations, *Philos. Trans. R. Soc. London Ser. A*, *338*, 169–236.

Larsen, J. C., and T. B. Sanford (1985), Florida Current volume transport from voltage measurements, *Science*, *227*(4684), 302–304.

Lien, R.-C., E. A. D'Asaro, and M. J. McPhaden (2002), Internal waves and turbulence in the upper central equatorial Pacific: Lagrangian and Eulerian observations, *J. Phys. Oceanogr.*, *32*(9), 2619–2639.

Longuet-Higgins, M. S., M. E. Stern, and H. Stommel (1954), The electrical fields induces by ocean currents and waves, with applications to the method of towed electrodes, *Pap. Phys. Oceanogr. Meteorol.*, *13*(1), 1–37.

Luther, D. S., and A. D. Chave (1993), Observing integrating variables in the ocean, in *Proceedings of the 7th Annual 'Aha Huliko'a Hawai'ian Winter Workshop on Statistical Methods in Physical Oceanography*, edited by P. Müller and D. Henderson, pp. 103–129, Univ. of Hawaii at Mānoa, Honolulu.

Meinen, C. S., D. S. Luther, D. R. Watts, K. L. Tracey, A. D. Chave, and J. Richman (2002), Combining inverted echo sounder and horizontal electric field recorder measurements to obtain absolute velocity profiles, *J. Atmos. Oceanic Technol.*, *19*(10), 1653–1664.

Nash, J. D., E. Kunze, C. M. Lee, and T. B. Sanford (2006), Structure of the baroclinic tide generated at Kaena Ridge, Hawaii, *J. Phys. Oceanogr.*, *36*(6), 1123–1135.

Pawlak, G., P. MacCready, K. A. Edwards, and R. McCabe (2003), Observations on the evolution of tidal vorticity at a stratified deep water headland, *Geophys. Res. Lett.*, *30*(24), 2234, doi:10.1029/2003GL018092.

Preisendorfer, R. W., J. C. Larsen, and M. A. Sklarz (1974), Electromagnetic fields induced by plane-parallel internal and surface ocean waves, *Tech. Rep. HIG-74-7*, Hawaii Inst. of Geophys. and Planetol., Univ. of Hawaii at Mānoa, Honolulu.

Sanford, T. B. (1971), Motionally induced electric and magnetic fields in the sea, *J. Geophys. Res.*, *76*(15), 3476–3492.

Sanford, T. B., R. G. Drever, and J. H. Dunlap (1978), A velocity profiler based on the principles of geomagnetic induction, *Deep Sea Res.*, *25*(2), 183–210.

Sanford, T. B., R. G. Drever, J. H. Dunlap, and E. A. D'Asaro (1982), Design, operation, and performance of an expendable temperature and velocity profiler (XTVP), *Tech. Rep. 8110*, Appl. Phys. Lab., Univ. of Wash., Seattle, Wash.

Sanford, T. B., R. G. Drever, and J. H. Dunlap (1985), An acoustic doppler and electromagnetic velocity profiler, *J. Atmos. Oceanic Technol.*, *2*(2), 110–124.

Sanford, T. B., J. F. Price, J. B. Girton, and D. C. Webb (2007), Highly resolved observations and simulations of the ocean response to a hurricane, *Geophys. Res. Lett.*, *34*, L13604, doi:10.1029/2007GL029679.

Simpson, F., and K. Bahr (2005), *Practical Magnetotellurics*, 251 pp., Cambridge Univ. Press, Cambridge, U. K.

Spain, P., and T. B. Sanford (1987), Accurately monitoring the Florida Current with motionally induced voltages, *J. Mar. Res.*, *15*(4), 599–608.

Szuts, Z. B. (2004), Electric field floats in the North Atlantic Current: Validation and observations, M.Sc. thesis, Sch. of Oceanogr., Univ. of Wash., Seattle, Wash.

Szuts, Z. B. (2008), The interpretation of motionally induced electric fields in oceans of complex geometry, Ph.D. thesis, Sch. of Oceanogr., Univ. of Wash., Seattle, Wash.

Szuts, Z. B. (2010), Relationship between ocean velocity and motionally induced electrical signals: 2. In the presence of topographic slopes, *J. Geophys. Res.*, *115*, C06004, doi:10.1029/2009JC006054.

Tyler, R. H. (2005), A simple formula for estimating the magnetic fields generated by tsunami flow, *Geophys. Res. Lett.*, *32*, L09608, doi:10.1029/2005GL022429.

Tyler, R. H., and L. A. Mysak (1995a), Motionally-induced electromagnetic fields generated by idealized ocean currents, *Geophys. Astrophys. Fluid Dyn.*, *80*, 167–204.

Tyler, R. H., and L. A. Mysak (1995b), Electrodynamics in a rotating frame of reference with application to global ocean circulation, *Can. J. Phys.*, *73*, 393–402.

Tyler, R. H., L. A. Mysak, and J. M. Oberhuber (1997), Electromagnetic fields generated by a 3-D global ocean circulation, *J. Geophys. Res.*, *102*(C3), 5531–5551.

Tyler, R. H., S. Maus, and H. Lühr (2003), Satellite observations of magnetic fields due to ocean tidal flow, *Science*, *299*, 239–241.

Tyler, R. H., F. Vivier, and S. Li (2004), Three-dimensional modelling of ocean electrodynamics using gauged potentials, *Geophys. J. Int.*, *158*, 874–887.

Wilson, D. W., and W. E. Johns (1997), Velocity structure and transport in the Windward Islands Passages, *Deep Sea Res. Part I*, *44*(3), 487–520.

Z. B. Szuts, Max-Planck-Institut für Meterologie, Bundesstr. 53, D-20146 Hamburg, Germany. (zoltan.szuts@zmaw.de)